The Astrophysical Journal, 696:182–191, 2009 May 1 doi:10.1088/0004-637X/696/1/182

SPECTROSCOPIC SIGNATURES OF THE SUPERORBITAL PERIOD IN THE NEUTRON STAR BINARY LMC X-4

Joseph Neilsen[1,2], Julia C. Lee[1,2], Michael A. Nowak[3], Konrad Dennerl[4], and Saeqa Dil Vrtilek[2]
[1] Astronomy Department, Harvard University, Cambridge, MA 02138, USA; jneilsen@cfa.harvard.edu
[2] Harvard-Smithsonian Center for Astrophysics, Cambridge, MA 02138, USA
[3] MIT Kavli Institute for Astrophysics and Space Research, Cambridge, MA 02139, USA
[4] Max-Planck-Institut für extraterrestrische Physik, Giessenbachstraße, 85748 Garching, Germany
Received 2008 July 21; accepted 2009 February 4; published 2009 April 14

ABSTRACT

We present the first high-resolution X-ray study of emission line variability with superorbital phase in the neutron star binary LMC X-4. Our analysis provides new evidence from X-ray spectroscopy confirming accretion disk precession as the origin of the superorbital period. The spectra, obtained with the *Chandra* High-Energy Transmission Grating Spectrometer and the *XMM-Newton* Reflection Grating Spectrometer, contain a number of emission features, including lines from hydrogen-like and helium-like species of N, O, Ne, and Fe, a narrow O VII radiative recombination continua (RRCs), and fluorescent emission from cold Fe. We use the narrow RRC and the Heα triplets to constrain the temperature and density of the (photoionized) gas. By comparing spectra from different superorbital phases, we attempt to isolate the contributions to line emission from the accretion disk and the stellar wind. There is also evidence for highly ionized iron redshifted and blueshifted by $\sim$25,000 km s^{-1}. We argue that this emission originates in the inner accretion disk and show that the emission line properties in LMC X-4 are natural consequences of accretion disk precession.

Key words: accretion, accretion disks – binaries: close – pulsars: individual (LMC X-4) – stars: neutron – X-rays: binaries

Online-only material: color figure

1. INTRODUCTION

The eclipsing binary LMC X-4 consists of a 1.25 $M_\odot$ accretion-powered X-ray pulsar orbiting a 14.5 $M_\odot$ O8 III star with a period of 1.4 days (Kelley et al. 1983; van der Meer et al. 2007). The system exhibits a 13.5 s pulsation due to the spin of the neutron star and a long-period superorbital variation of approximately 30 days (Lang et al. 1981; Ilovaisky et al. 1984), over which the X-ray flux may vary by as much as a factor of 60. Similar behavior has been observed in other X-ray binaries (Her X-1, Giacconi et al. 1973; SMC X-1, Gruber & Rothschild 1984).

The standard model for the superorbital period in LMC X-4 is a precessing accretion disk that periodically obscures the neutron star (Heemskerk & van Paradijs 1989). For high-luminosity systems, radiation pressure can generate a stable warp in the accretion disk, which then precesses due to radiation torque (Pringle 1996). During the low state, an observer views the edge of the disk and the neutron star is obscured; during the high state, the disk face is revealed and the neutron star is visible (Petterson 1977). Signatures of this obscuration are well documented in timing (Her X-1, Petterson et al. 1991; SMC X-1, Hickox & Vrtilek 2005; Neilsen et al. 2004) and broadband spectral (SMC X-1, Vrtilek et al. 2001; LMC X-4, Woo et al. 1995) studies of pulsar binaries. Furthermore, high-resolution X-ray studies of the accretion disk corona in Her X-1 indicate that the disk is in fact observed edge-on during the low state (Jimenez-Garate et al. 2005).

There is also substantial evidence to suggest that emission lines in Her X-1 and LMC X-4 vary with superorbital phase Ψ (Jimenez-Garate et al. 2002, hereafter JG02; Naik & Paul 2003, 2004). However, the relationship between lines and the continuum is complex and may require contributions from the accretion column, the accretion disk, a radiatively driven stellar wind, or an X-ray heated wind from the accretion disk atmosphere. The extent to which these emission lines vary with Ψ depends on the true physical origin of the superorbital period.

High-resolution spectroscopy is necessary to decompose the spectrum of LMC X-4 into its physical components. Particularly useful is the Heα emission line triplet (from helium-like ions). This triplet consists of the closely spaced resonance line (r: $1s^2\ ^1S_0$–$1s2p\ ^1P_1$), intercombination lines (i: $1s^2\ ^1S_0$–$1s2p\ ^3P_{2,1}$), and the forbidden line (f: $1s^2\ ^1S_0$–$1s2s\ ^3S_1$). The ratio $R = f/i$ can be used to determine the electron density of the emitting plasma for 10^8 cm$^{-3} < n_e < 10^{18}$ cm^{-3}, and $G = (f + i)/r$ is sensitive to the electron temperature in the range 10^6 K $< T_e < 10^7$ K (Gabriel & Jordan 1969; Porquet & Dubau 2000). Furthermore, because photo- and collisional excitation populate atomic levels differently, these line ratios can be used to infer the dominant excitation mechanism in astrophysical plasmas.

We have carried out detailed spectral analysis of the first high-resolution X-ray grating spectra of LMC X-4, obtained with the *Chandra* High-Energy Transmission Grating Spectrometer (HETGS; Canizares et al. 2005) and the *XMM-Newton* Reflection Grating Spectrometer (RGS; den Herder et al. 2001). These observations probe the transition from the low state to the high state of the superorbital period, revealing the physical processes at work. We present the first study of the plasma conditions in LMC X-4 with density and temperature diagnostics from helium-like species; we exploit the variability of these lines to constrain the geometry and dynamics of the line-emitting regions. In Section 2, we describe the observations and data reduction; in Section 3, we discuss continuum fitting and line searches. We present and interpret the emission lines from LMC X-4 in Sections 4 and 5, and conclude in Section 6.

Table 1
Observations of LMC X-4

Obs. ID	X-ray State	Grating	Start Time[a]	T_{exp} (ks)	Orbital Phase[b]
0142800101	High	RGS	52891.42	113.5	0.25–1.19
9573	Transition	HETGS	54342.08	44.1	0.28–0.71
9574	Transition	HETGS	54343.45	51.0	0.25–0.62
9571	Transition	HETGS	54344.68	47.1	0.12–0.53

Notes.
[a]MJD = JD-2,400,000.5.
[b]Computed from the ephemeris of Levine et al. (2000).

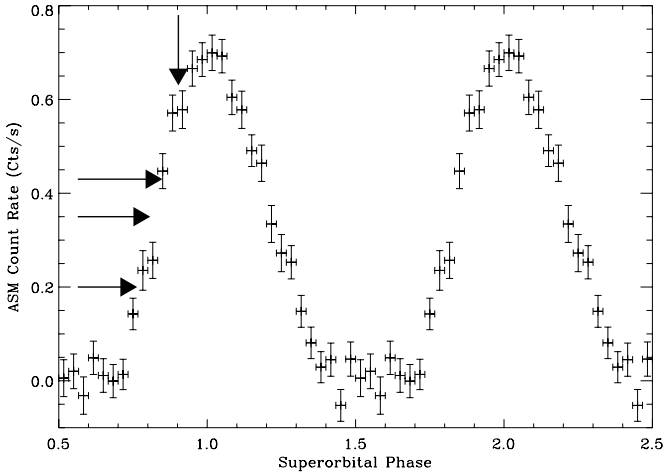

Figure 1. *RXTE*/ASM light curve of LMC X-4, folded on the long-term period of 30.3 days; two cycles are shown for clarity. $\Psi = 1$ is defined to be the peak of the high state. The *Chandra* HETGS grating observations of the state transition are shown as horizontal arrows, and the *XMM-Newton* RGS observation of the high state is shown as a vertical arrow.

2. OBSERVATIONS AND DATA REDUCTION

LMC X-4 was observed with the RGS on *XMM-Newton* on 2003 September 9 (10:11:34 UT) for 113.5 ks (approximately one full orbital period). This observation took place during the high state of the 30 days superorbital cycle. The transition from the low state to the high state was observed with the *Chandra* HETGS on 2007 August 30 (01:52:21 UT), August 31 (10:49:17 UT), and September 1 (16:18:44 UT) for 47.09 ks, 50.96 ks, and 44.06 ks, respectively, for a total exposure time of 142.11 ks on the source. The observations are reported in Table 1 and are shown with respect to the superorbital period in Figure 1.

The RGS data were processed with SAS version 7.1.0 and standard data reduction tools. We obtained spectra from RGS-1 and RGS-2 with FWHM spectral resolutions of roughly $\Delta\lambda = 0.06$ Å. Bad columns, including CCD chip 7 in RGS-1 and CCD chip 4 in RGS-2, were flagged and subsequently ignored. We also extracted the EPIC-PN spectrum in order to constrain the power-law index above 3 keV in the high state. The EPIC-PN spectrum will be analyzed in a future paper (K. Dennerl 2009, in preparation). For reasons to be discussed in Section 4.1, we also extracted a separate RGS spectrum of LMC X-4 during eclipse.

The HETGS data were analyzed with the CIAO analysis suite, version 3.4.3. After reprocessing and filtering the data, we extracted medium energy grating (MEG) and high energy grating (HEG) spectra, which have FWHM spectral resolutions of 0.023 Å and 0.012 Å, respectively. Because the *destreak* tool can cause spectral artifacts for bright sources, we used the order-sorting routine to remove the ACIS S-4 streak. To achieve sufficient signal-to-noise ratio (S/N), we combined all three HETGS observations. This may involve averaging over real phenomena, but the third observation is close to an order of magnitude brighter than the other two combined, so the effect should be small. In general, we do not account for orbital variability. We performed the following spectral analysis in the Interactive Spectral Interpretation System (ISIS) (Houck & Denicola 2000; Houck 2002).

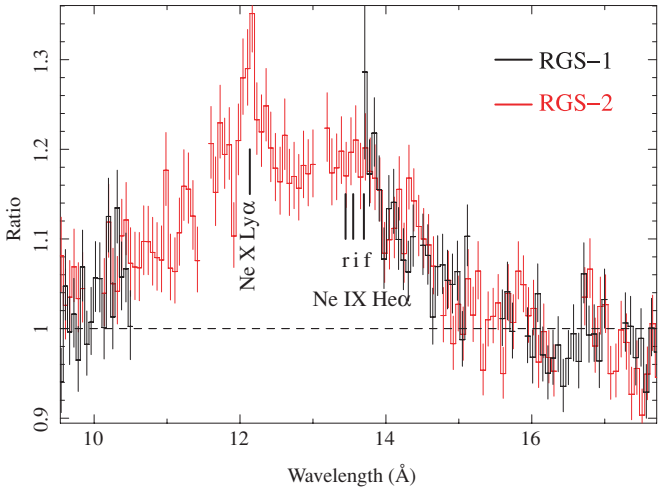

Figure 2. Data:model ratio for the RGS spectra near 12 Å, showing the broad bump and the location of emission features from H- and He-like Ne. The bump obscures the Ne IX lines and prevents a completely reliable determination of the Ne X line flux. In our continuum fits, we model it as a broad Gaussian with $\Delta\lambda \sim 1.3$ Å and equivalent width $W_0 \sim 60$ eV.
(A color version of this figure is available in the online journal.)

3. CONTINUUM SPECTROSCOPY AND LINE SEARCHES

Historically, the X-ray continuum in LMC X-4 has been modeled as an absorbed hard power law plus a soft excess, which is evident because of the low N_H toward the LMC (Hickox et al. 2004). The power law likely consists of Comptonized photons from the neutron star. Its slope varies between $\Gamma \sim 0.5$ and 0.7; the soft excess has been described as a combination of thermal Comptonization (La Barbera et al. 2001), blackbody radiation (Naik & Paul 2002), and thermal bremsstrahlung (Naik & Paul 2004). We set the minimum N_H at the Galactic value, 5.78×10^{20} cm^{-2} (Dickey & Lockman 1990) and fit the spectra with various combinations of these hard and soft components.

However, we are unable to find a completely physical model for the high-state continuum due to a broad bump near 12 Å (see Figure 2; also see JG02 for a discussion of possible origins for this feature in Her X-1). This bump is apparent in both RGS detectors. We model it as a Gaussian with width $\Delta\lambda \sim 1.3$ Å and equivalent width $W_0 \sim 60$ eV. For this reason, we will refrain from drawing any significant physical inferences from our continuum model. In order to achieve $\chi^2_\nu \lesssim 3.4$ (degree of freedom (dof) 565) in the RGS, it is necessary to include narrow Gaussians to model the spectral lines. We include 10 Gaussian components: six for the helium-like triplets of nitrogen and oxygen, two for the Lyα lines of nitrogen, oxygen, and two unidentified strong absorption lines. The bump prevents reliable analysis of the Ne IX triplet and the Ne X Lyα line. We let the fluxes of the Gaussian lines vary when fitting the continuum, then fit all the line parameters separately.

Among those tested, the best spectral model for the high-state data is thermal bremsstrahlung with $kT_{\rm bremss} = 0.455^{+0.022}_{-0.001}$ keV plus the broad Gaussian bump, the narrow lines, a blackbody with $kT_{\rm bb} = 43.4^{+1.7}_{-0.2}$ eV and a power law with $\Gamma = 0.813 \pm 0.007$ (constrained by the EPIC spectrum above 3 keV), absorbed by the Galactic neutral hydrogen column ($N_{\rm H} = 5.78 \times 10^{20}$ cm^{-2}). The absorption lines, which may be interstellar in origin, are found at $23.541^{+0.002}_{-0.030}$ Å and $23.7^{+0.4}_{-1.7}$ Å, and have equivalent widths of -0.96 ± 1.4 eV and $-0.21^{+0.19}_{-0.18}$ eV, respectively. This model results in $\chi^2_\nu = 1.55$ (dof 537), which is not formally acceptable, but there is very little structure in the residuals and it is not our goal to model every spectral feature in the RGS.

Because the *Chandra* and *XMM-Newton* observations probe different X-ray states of LMC X-4, we fit their continuum parameters separately. Unfortunately, there is insufficient S/N in the MEG/HEG to constrain the column density independently, so in fitting the HETGS spectrum we fix $N_{\rm H}$ at the Galactic value (also measured by the RGS). To ensure that our characterization of the continuum is accurate given the low S/N, we group the data to a minimum of 40 counts per bin and include a Gaussian emission line to account for the strong Fe Kα line at 6.4 keV. The best fit for the HETGS data from 0.5–10 keV is bremsstrahlung with $kT = 0.43 \pm 0.03$ keV plus a shallow power law with $\Gamma = 0.40 \pm 0.04$. The iron line appears at 1.941 ± 0.002 Å and has $W_0 = 130 \pm 30$ eV; the model gives $\chi^2_\nu = 1.21$ for 886 dof. Assuming a distance of 50 kpc to LMC X-4, we measure unabsorbed continuum luminosities of (0.5–10 keV) $L_{\rm X} = 1.2 \times 10^{37}$ erg s^{-1} in the state transition and $L_{\rm X} = 1.0 \times 10^{38}$ erg s^{-1} in the high state.

After finding a satisfactory continuum model for the HETGS, we proceed to model the spectral lines. We include Gaussian components for the triplets from helium-like species of oxygen, neon, and iron as well as Lyα lines from hydrogen-like nitrogen, oxygen, neon, and iron (these were the strongest lines visible in our spectra), and find 90% confidence limits. Because of somewhat low S/N, we find it necessary to rebin the MEG spectrum to 0.092 Å (four times worse than the nominal resolution) for $\lambda > 16$ Å; the rest of the data are binned to the nominal resolution. Our final fit gives $\chi^2_\nu = 1.08$ for 1758 dof. We show the line parameters in Table 2. The RGS-1 and RGS-2 spectra are plotted in Figure 3, and the MEG spectrum is plotted in Figure 4. The RGS eclipse spectrum is plotted in Figure 5.

In order to confirm our line IDs, we perform simple checks with analytic photoionization models from XSTAR, using a power law with $\Gamma = 0.4$ as our ionizing spectrum (Kallman & McCray 1982). We compare our spectrum with the XSTAR predictions for other lines and adjust the model to fit for the appropriate line redshifts and intensities. In this way, we are able to estimate the dynamics and ionization state of the emitting plasma. In the case of the narrow iron lines in the HETGS, we find evidence for lines separated from Fe XXV by ~25,000 km s^{-1}. In order to assess the possibility that these lines correspond to a physical Doppler shift, we search for similar Doppler shifts of our other lines as well. This process results in a total of 21 Gaussian emission lines (stationary or Doppler shifted) and two radiative recombination continua (RRCs) in the HETGS.

4. EMISSION LINES

The line emission from LMC X-4 is dominated by hydrogen- and helium-like ions. In particular, the transition-phase HETGS and the high-state RGS spectra contain narrow emission lines from N VI, N VII, O VII, O VIII, Ne IX, and Ne X. Because of the absence of L-shell iron emission lines and the presence of RRCs from N VI and O VII (HETGS only), we conclude that these are recombination cascade emission lines. As can be seen from Table 2, these lines are all consistent with little or no Doppler velocity. In the helium-like triplets, the intercombination (*i*) line dominates. We will discuss line ratios in Section 4.2. In the transition phase, we detect a strong fluorescent Fe Kα emission line and recombination lines from Fe XXV and Fe XXVI.

A comparison of the transition-phase and high-state spectra yields an interesting discovery: emission lines from helium-like nitrogen, oxygen, and neon do not evolve in the same way as emission lines from the corresponding hydrogen-like species. Our analysis leads us to the conclusion that at least three emission regions are necessary to explain the line properties in LMC X-4. In the next sections, we will summarize this argument and discuss each region individually. Because of chip defects in the RGS (20–24 Å and 10.6–13.8 Å for RGS-2 and RGS-1, respectively) and low S/N in the MEG, we will focus on the O VII triplet when discussing helium-like species. Note also that the emission lines are grouped according to region in Table 2.

4.1. Line Evolution

The most striking feature of the variable emission lines in LMC X-4 is that while the emission from N VII and O VIII is highly correlated with the continuum flux, the emission from N VI and O VII is not. In particular, while the equivalent widths of the Lyα lines from hydrogen-like N and O appear to be independent of superorbital phase (at the 90% confidence level), the equivalent widths of lines from the corresponding helium-like species decrease substantially when the continuum flux increases. Interestingly, the flux in the helium-like lines appears to be constant over superorbital phase.

For example, O VIII Lyα has $W_0 = 4.1^{+2.9}_{-2.2}$ eV as measured by the HETGS in the transition and $W_0 = 4.7 \pm 0.4$ eV as detected by the RGS in the high state. In comparison, the equivalent width of the O VII *i* line decreases by a factor of ~13, from $W_0 = 11.5^{+4.7}_{-3.6}$ eV in the transition (HETGS) to $W_0 = 0.9^{+0.3}_{-0.2}$ eV in the high state (RGS). The flux in this line, however, does not change: we measure (in units of 10^{-5} photons s^{-1} cm^{-2}) $f = 13.3^{+5.5}_{-4.2}$ in the transition (HETGS) and $f = 12.6^{+3.4}_{-3.3}$ in the high state (RGS).

Further comparison of the transition state spectra to the high-state spectra reveals a noticeable increase in the broadening of these hydrogen-like Lyα lines relative to their helium-like counterparts: the helium-like triplets have no significant velocity width in either the transition or the high state. In the high state, the N VII and O VIII Lyα lines have $\sigma_v = 1370$ km s^{-1} and 2270 km s^{-1}, respectively. Because the RGS is able to constrain the width of narrower lines (N VII is narrower than 370 km s^{-1} in the high state), we believe that this broadening is real. If it is thermal in origin, the implied temperature is $T \sim 10^9$ K; Doppler broadening arising from bulk motion is more likely. These values should be compared to the transition-phase widths, which are <330 km s^{-1} for N VII and 820 km s^{-1} for O VIII.

These results are difficult to reconcile with a single emission region with a variable ionization state. The fact that the hydrogen-like lines brighten by the same factor as the continuum while the helium-like lines do not change suggests that the hydrogen- and helium-like lines are produced independently,

Table 2
X-ray Emission Lines in LMC X-4

Line(s)	λ_0 (Å)	λ (Å)	$\Delta v_{\rm shift}$ (km s^{-1})	Flux	W_0 (eV)	σ_v (km s^{-1})	Grating
Region I: X-ray irradiated stellar wind							
Ne IX Heα	13.447 (*r*)	···	···	<0.8	$1.0^{+1.3}_{-0.9}$	···	HETG
	13.552 (*i*)	$13.560^{+0.004}_{-0.001}$	190^{+100}_{-30}	$1.7^{+0.6}_{-0.5}$	$5.0^{+1.8}_{-1.5}$	<704	HETG
	13.698 (*f*)	···	···	<0.6	<1.7	···	HETG
O VII RRC	16.78	···	···	<1.8	$1.4^{+1.7}_{-1.3}$	···	HETG
O VII Heβ	18.63	18.65 ± 0.04	280^{+580}_{-600}	$3.4^{+2.1}_{-1.6}$	$4.3^{+2.6}_{-2.1}$	700^{+550}_{-340}	HETG
O VII Heα	21.602 (*r*)	$21.633^{+0.007}_{-0.063}$	440^{+100}_{-870}	$6.0^{+4.1}_{-2.8}$	$5.3^{+3.6}_{-2.5}$	<620	HETG
		···	···	<4.9	<0.4	···	RGS
	21.802 (*i*)	21.805 ± 0.005	40 ± 70	$13.3^{+5.5}_{-4.2}$	$11.5^{+4.7}_{-3.6}$	<400	HETG
		$21.84^{+0.04}_{-0.02}$	470^{+500}_{-270}	$12.6^{+3.4}_{-3.3}$	$0.9^{+0.3}_{-0.2}$	<1030	RGS
	22.10 (*f*)	···	···	<4.0	<3.3	···	HETG
		···	···	$3.7^{+3.3}_{-3.2}$	0.3 ± 0.2	···	RGS
N VI RRC	22.46	22.52 ± 0.08	810^{+1080}_{-1040}	<7.6	<6.1	···	HETGS
N VI Heα	28.78 (*r*)	···	···	<6.5	<0.2	···	RGS
	29.08 (*i*)	29.11 ± 0.02	230 ± 190	$19.4^{+3.8}_{-3.7}$	0.6 ± 0.1	<370	RGS
	29.53 (*f*)	···	···	<6.3	<0.2	···	RGS
Region II: outer accretion disk							
Fe XXVI Lyα	1.781	$1.785^{+0.008}_{-0.012}$	710^{+1280}_{-2100}	<1.4	<33.2	···	HETG
Fe XXV Heα[a]	1.850 (*r*)	$1.869^{+0.009}_{-0.006}$	3050^{+1510}_{-1060}	$3.7^{+1.2}_{-1.1}$	$86.5^{+28.6}_{-25.7}$	3180^{+1560}_{-1120}	HETG
	1.857 (*i*)	···	1910^{+1500}_{-1050}	···	···	···	HETG
	1.868 (*f*)	···	180^{+1480}_{-1040}	···	···	···	HETG
Fe Kα	1.938	$1.941^{+0.002}_{-0.002}$	470^{+330}_{-370}	$5.8^{+1.1}_{-1.0}$	$135.2^{+25.3}_{-23.0}$	1200^{+430}_{-330}	HETG
Ne X Lyα	12.135	$12.158^{+0.002}_{-0.003}$	580^{+40}_{-80}	0.9 ± 0.3	$3.3^{+1.3}_{-1.1}$	280^{+190}_{-200}	HETG
O VIII Lyα	18.97	18.97 ± 0.05	-20^{+760}_{-720}	$3.3^{+2.3}_{-1.8}$	$4.1^{+2.9}_{-2.2}$	820^{+880}_{-400}	HETG
		18.95 ± 0.02	-250 ± 280	45.6 ± 3.7	4.7 ± 0.4	2270^{+320}_{-290}	RGS
N VII Lyα	24.78	$24.79^{+0.05}_{-0.02}$	50^{+600}_{-190}	$7.5^{+4.2}_{-3.0}$	$4.8^{+2.7}_{-1.9}$	<330	HETG
		24.79 ± 0.02	110 ± 180	$58.4^{+5.1}_{-5.0}$	3.1 ± 0.3	1370^{+200}_{-180}	RGS
Region III: inner accretion disk							
Fe XXV Heα[a]	1.850 (*r*)	$1.710^{+0.006}_{-0.008}$	-23560^{+910}_{-1180}	$1.8^{+1.2}_{-1.0}$	$43.1^{+29.4}_{-24.6}$	<4320	HETG
	1.857 (*i*)	···	-24690^{+900}_{-1170}	···	···	···	HETG
	1.868 (*f*)	···	-26410^{+890}_{-1160}	···	···	···	HETG
Fe XXV Heα[a]	1.850 (*r*)	$2.005^{+0.006}_{-0.008}$	23950^{+1120}_{-1400}	$1.5^{+0.8}_{-0.7}$	$33.8^{+17.8}_{-15.6}$	1910^{+2240}_{-1380}	HETG
	1.857 (*i*)	···	22820^{+1110}_{-1390}	···	···	···	HETG
	1.868 (*f*)	···	21100^{+1100}_{-1380}	···	···	···	HETG
O VII Heβ	18.63	$20.61^{+0.07}_{-0.01}$	30220^{+1140}_{-270}	$3.6^{+3.1}_{-2.1}$	$3.5^{+3.1}_{-2.1}$	< 930	HETG
O VIII Lyα	18.97	$17.36^{+0.05}_{-0.04}$	-26570^{+740}_{-620}	<1.8	<2.8	< 5200	HETG
		$20.92^{+0.01}_{-0.07}$	29190^{+260}_{-1060}	$3.1^{+3.2}_{-2.2}$	$2.9^{+3.0}_{-2.1}$	< 1100	HETG
O VII Heα	21.602 (*r*)	$19.91^{+0.06}_{-0.03}$	-24450^{+840}_{-370}	3.0	<3.3	···	HETG
	21.802 (*i*)	$20.13^{+0.09}_{-0.02}$	-23970^{+1250}_{-110}	$2.0^{+2.6}_{-1.8}$	$2.1^{+2.8}_{-1.9}$	<3450	HETG
N VII Lyα	24.78	$22.91^{+0.02}_{-0.06}$	-23470^{+130}_{-670}	$8.6^{+8.7}_{-5.3}$	$6.6^{+6.7}_{-4.0}$	<2000	HETG

Notes. Errors quoted are 90% confidence ranges for a single parameter. λ_0: rest wavelength; λ: measured wavelength; $\Delta v_{\rm shift}$: measured Doppler velocity; flux: measured line flux in units of 10^{-5} photons s^{-1} cm^{-2}; W_0: line equivalent width; σ_v: measured line width. The high state was probed by the RGS, and the transition phase was observed with the HETGS (see Figure 1). Notice that the lines from Regions I and II are all consistent with a very small Doppler velocity (as long as Fe XXV in the high state is dominated by the forbidden line—see Section 4.3).

[a]Because the Fe XXV triplet is unresolved, we report the Fe XXV line with three velocities, which correspond to the iron velocity assuming the line is dominated by the resonance line, the intercombination line, or the forbidden line, respectively.

probably in two distinct emission regions with different ionization states. The fact that the O VIII line weakens relative to the O VII triplet during eclipse (compare Figures 3 and 5) also supports at least two emission regions. The presence of high-velocity ($\sim$25,000 km s^{-1}) iron during the state transition implies that a third region may be necessary to explain all the lines in LMC X-4.

The first region (hereafter Region I), is defined as the source of the helium-like triplets and weak hydrogen-like lines (note that this refers only to N, O, and Ne). The luminosity of Region I is not affected by superorbital variations in the X-ray flux; if it consists of a photoionized plasma, this might indicate that its luminosity is tied to the intrinsic luminosity of the neutron star. Region II is the source of the strong Lyα lines, whose intensity

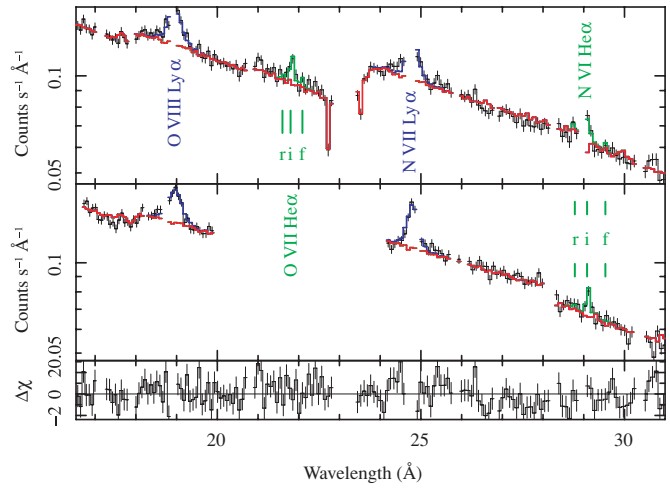

Figure 3. RGS high-state spectrum of LMC X-4; RGS-1 is plotted in the top panel and RGS-2 is plotted in the center panel. Note the strong O VIII and N VII Lyα lines at 18.97 Å and 24.78 Å, respectively. Gaps in the spectra correspond to ignored columns. The red, green, and blue models correspond to the continuum, Region I, and Region II spectra. We show the residuals for RGS-1 in the bottom panel.

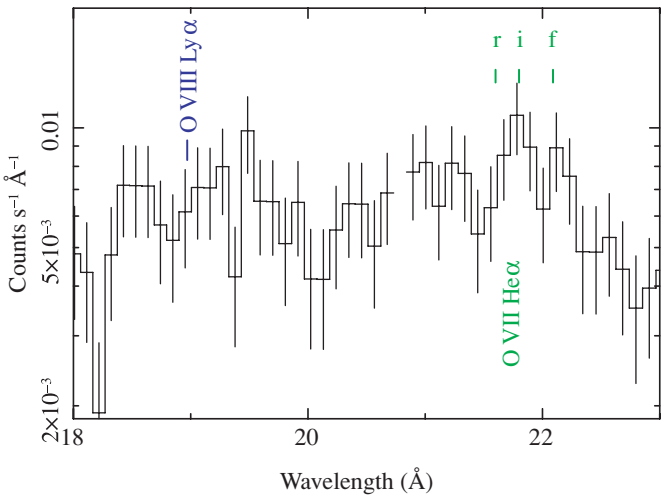

Figure 5. RGS-1 eclipse spectrum of LMC X-4. During the eclipse, the O VIII Lyα line weakens relative to the O VII triplet, indicating that Region II is not visible during eclipse. Given that Region II is highly ionized, exhibits somewhat broadened emission lines, and is obscured during eclipse, we argue that it is located in the accretion disk.

is tied to the observed X-ray continuum. This region makes little or no contribution to the helium-like triplets. Region III, for reference, is the origin of the Doppler-shifted Fe XXV lines.

4.2. Region I: The X-ray Irradiated Stellar Wind?

As discussed in the preceding section, we define Region I as the origin of the helium-like emission triplets. These triplets are useful for plasma diagnostics because their R and G line ratios can constrain the density, temperature, and dominant ionization process in the emitting plasma. Given the striking differences between line evolution in Regions I and II, these quantities are particularly important for a complete description of this high-mass binary.

In N VI, O VII, and Ne IX, we observe prominent intercombination lines, weak-to-moderate resonance lines, and weak forbidden lines; for all these species, $R \sim 0$ (with upper limits of $\sim$0.5 at 90% confidence). Collisions can produce this line ratio by exciting the $2^3S_1 \rightarrow 2^3P_{1,2}$ transition, effectively converting forbidden-line photons into intercombination line photons. Thus, if collisional ionization dominates, it is possible to find lower limits on n using the upper limits on R from the values in Table 2 and the relationship between R and n determined by Porquet & Dubau (2000). With this method, $R \sim 0$ implies a high-density plasma in Region I.

However, photoexcitation by the intense UV field of the secondary can compete with collisional excitation to produce

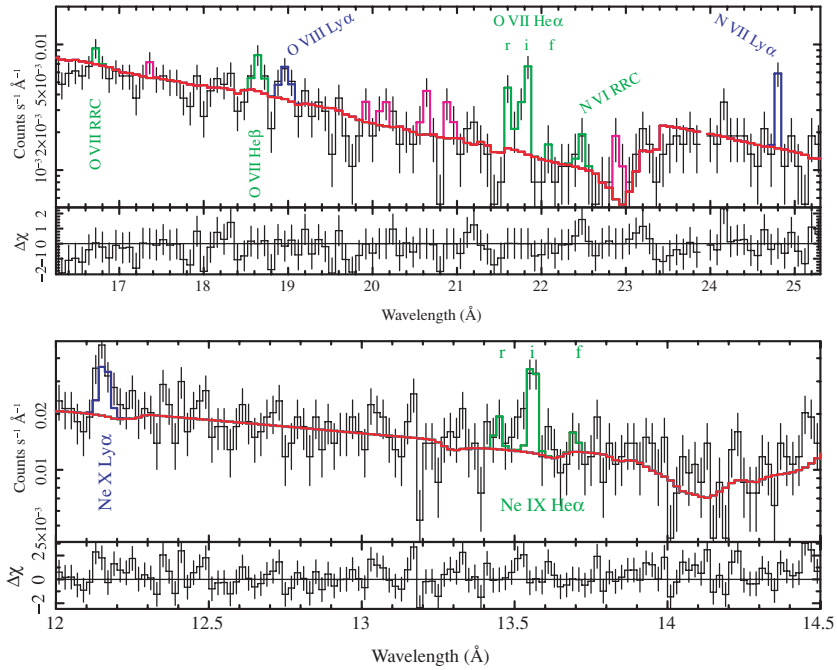

Figure 4. MEG transition-phase equivalent of Figure 3 showing data, fit, and residuals; again the red, green, blue, and magenta models correspond to the continuum, Regions I, II, and III, respectively. We have labeled the strongest lines.

$R \sim 0$ (Mewe & Schrijver 1978). The photoexcitation rate is given by

$$w_{f\to i} = \frac{\pi e^2}{mc} F_{\nu_{f\to i}} f_{\rm osc}, \quad (1)$$

where m and e are the mass and charge of the electron, c is the speed of light, $f_{\rm osc}$ is the oscillator strength, and $F_{\nu_{f\to i}}$ is the flux (in units of photons s^{-1} cm^{-2} Hz^{-1}) at the wavelength of the $2^3S_1 \to 2^3P_{1,2}$ transition (1637 Å for O VII). Following JG02, we assume a UV point source (so that the radiation field and photoexcitation rate $w_{f\to i}$ decrease with the square of the distance d from the secondary) and calculate the distance $d_{\rm crit}$ at which the photoexcitation rate equals the radiative decay rate w_f. Inside $d_{\rm crit}$, photoexcitation destroys forbidden-line photons, so the density limits from $R \sim 0$ are not applicable.

At orbital phase 0.74 (similar to our observations) and superorbital phase between 0.8 and 1.1 (i.e., in the low-to-high-state transition or in the high state), Preciado et al. (2002) measured the UV flux at 1637 Å to be $F_{\lambda_{f\to i}} = 2.2\pm0.3\times10^{-13}$ erg s^{-1} cm^{-2} Å^{-1}. Taking the radiative decay rate and oscillator strength for O VII from Drake (1971) and Cann & Thakkar (1992), respectively, we calculate $d_{\rm crit} \sim 3\times10^{13}$ cm. This is much larger than the orbital separation $a = 9.3\times10^{11}$ cm (van der Meer et al. 2007), so photoexcitation cannot be ignored in explaining $R \sim 0$. If we neglect collisions altogether, so that $R \sim 0$ is produced by photoexcitation alone, we find that $R_{\rm I} \lesssim d_{\rm crit}$ (we can ignore the orbital separation because it is much smaller than $d_{\rm crit}$). We conclude that R cannot be used to constrain the density of Region I.

It should also be possible to constrain the density using the G ratio, because at high densities the resonance line is enhanced by collisional depopulation of the $1s2s\ ^1S_0$ level. This effect results in a measurable decrease in G for $n \gtrsim 10^{12}$ cm^{-3} for O VII (Gabriel & Jordan 1972). We attempt to account for collisions by modeling the spectrum with XSTAR. We fit the O VII triplet with a grid of models in n and ξ, covering $1 \leqslant \log\xi \leqslant 2$ and $\log(n/{\rm cm}^{-3}) = \{11, 12, 13, 14, 15, 16\}$, but find that the relatively low S/N of the HETGS spectra does not permit a statistically robust constraint on n.

G can also be used to determine the ionization mechanism in Region I. In the low-density limit, $G = 4$ is the cutoff between photoionized and collisional plasmas; $G > 4$ indicates that photoionization dominates (Porquet & Dubau 2000). This cutoff is somewhat lower at high density. Because the r line is a combination of recombination emission, resonant scattering into the line of sight, and resonant absorption, G should be interpreted with care (Wojdowski et al. 2003). This is particularly true during the state transition (observed with *Chandra*), when the pulsar is at least partially obscured and resonant scattering into the line of sight is almost certainly important. In any case, the observed resonance lines in LMC X-4 are weak, and we are generally only able to place a lower bound on G. In the high state, we measure $G \gtrsim 2.0$ using N and O; in the transition, we find $G = 2.3^{+4.8}_{-1.4}$ and $G > 1.5$ for O VII and Ne IX, respectively. These values allow for photoionization dominance, but we are unable to use G alone to determine the dominant ionization process in LMC X-4.

However, the comparison of hydrodynamic disk and wind models against UV spectra has shown that photoionization of the stellar wind can explain the orbital variability of emission and absorption line profiles in LMC X-4 (Vrtilek et al. 1997; Boroson et al. 1999, 2001). Furthermore, we detect narrow RRC from N VI and O VII. In the narrow limit, the width of the RRC is proportional to the electron temperature. A joint fit to these two features indicates $kT \sim 1$ eV, or $T \sim 1.2\times10^4$ K. The RRCs are too faint to provide confidence limits on T with the `redge` model, but Gaussian fits (which are acceptable because the features are narrow) imply $\sigma < 4.3$ eV, or $T \lesssim 5\times10^4$ K. Because collisional ionization is negligible at these temperatures, photoionization must be the dominant process in Region I. For reference, the continuum emission from Region I falls below the spectral sensitivity of the HETGS and RGS.

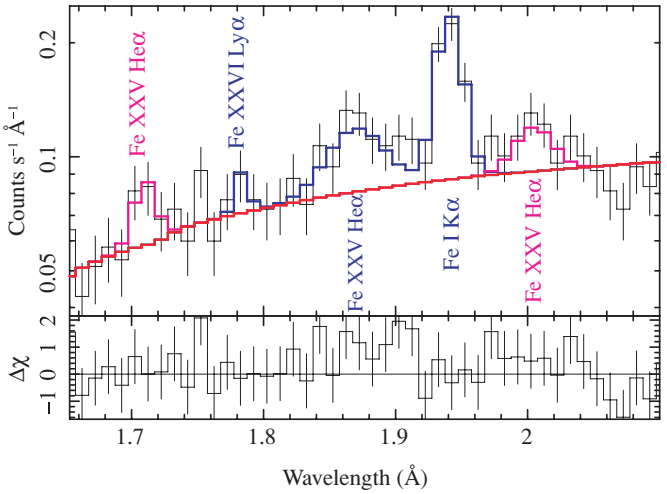

Figure 6. HEG transition-phase spectrum of the LMC X-4 iron region. The red line is the continuum fit; blue and magenta correspond to Regions II and III, respectively.

Given these results, we suggest that the X-ray irradiated stellar wind is a promising candidate for the identity of Region I. We have already mentioned that this component contributes significantly to the UV spectrum of LMC X-4, and we have seen that the temperature of Region I is typical of an O-type star. At this point, we cannot legitimately distinguish the stellar wind from the face of the secondary. However, the simplest explanation for the apparent absence of variability on the superorbital period in Region I is that it occupies a large solid angle as seen by the neutron star, and the stellar wind meets this criterion easily. We shall return to this topic in Section 5.

4.3. Region II: The Outer Accretion Disk/Stream?

Before discussing the Lyα lines from N VII, O VIII, and Ne X, it will prove useful to describe the iron lines in LMC X-4. During the state transition, we detect a number of iron emission lines. They are shown in Figure 6, with Gaussian parameters in Table 2. It is straightforward to identify three of these lines (at 6.4 keV, 6.7 keV, and 6.9 keV) as the Fe Kα complex, Fe XXV Heα, and Fe XXVI Lyα, respectively. If we assume that the Fe XXV emission is dominated by the forbidden line, then these three iron lines have the same velocity at 90% confidence, i.e., $v \sim 0$ km s^{-1}. This is a reasonable assumption because the critical density for Fe XXV is well above 10^{17} cm^{-3}, so its forbidden line will be strong for a very wide range of densities (Gabriel & Jordan 1972). Two other lines at 6.1 keV and 7.3 keV constitute Region III and will be addressed shortly.

XSTAR photoionization models of this spectral region which confirm our identification of Fe XXV Heα and Fe XXVI Lyα (see Section 3) indicate $\log\xi \sim 3$. At this ionization state, the contribution from helium-like species of N, O, and Ne is negligible. For the state transition in LMC X-4, XSTAR

predicts Lyα lines from N and O that are weaker than the Poisson noise in our spectra. Thus, the weak narrow Lyα lines that we detect during the state transition probably originate in Region I; their strong, broad counterparts in the high state originate in Region II. Disentangling the exact contributions to each line from these two regions is beyond the scope of this paper; full photoionization modeling will follow in future work.

At this point, we cannot proceed without associating the transition-phase iron lines with the high-state Lyα emission lines from N, O, and Ne. This association appears to be confirmed by the presence of the Fe Kα and Fe XXV lines in the EPIC high-state spectrum (K. Dennerl 2009, in preparation). Furthermore, the iron line model easily provides the high ionization parameter required by the absence of helium-like species in Region II. In addition, the comparable widths of the iron lines and the Lyα lines, along with their comparable small Doppler velocities, are consistent with a common origin. Thus, we shall treat all these lines as originating in Region II. Note that the Lyα lines become visible in the high state because of the correlation between the continuum flux and the flux from Region II.

Our association of hydrogen-like N, O, and Ne with a hotter region of the binary also explains the absence of RRC from these species during the high state. At an ionization parameter $\log \xi \sim 3$, the temperature in Region II is $T \gtrsim 5 \times 10^5$ K ($kT \gtrsim 50$ eV). The corresponding RRC would be very difficult to detect over the bright continuum of the high state. If the RRC normalizations follow the scaling of Liedahl & Paerels (1996), then the absence of a strong O VIII RRC implies $T > 10$ eV at 90% confidence. During the state transition, there is some evidence for a possible narrow O VIII RRC with $kT = 0.5$ eV ($T \sim 6000$ K). Given the above discussion, we suggest that this feature, if real, actually reflects the contribution of Region I to the Lyα lines.

Finally, we would like to determine the distance of Region II from the neutron star. We have an estimate for the ionization parameter in this region from the iron line model, but no density estimate. However, the fact that Region II is obscured during eclipse implies a distance from the neutron star of $R_{\rm II} \lesssim R_\star$, where $R_\star = 7.8\ R_\odot$ is the radius of the companion star (van der Meer et al. 2007). This is a weak constraint, but if we assume that the line broadening in Region II is due to orbital motion with a Keplerian velocity profile, then $R_{\rm II} \lesssim 1.5 \times 10^{11}$ cm, i.e., well inside the Roche lobe of the neutron star. We therefore conclude that Region II lies in the accretion disk. It should be pointed out that if the disk is cool and optically thick in the center but has a hot, optically thin surface layer, then it would be possible for both Fe XXV and cold iron (for the Fe Kα line) to be present in Region II. This would also explain their similar velocity dispersions and radial velocities but different ionization states. However, if the width of the Fe Kα line is due to a blend of several charge states, then the cold iron might lie outside of Region II.

4.4. Region III: The Inner Accretion Disk?

In addition to the three iron lines from Region II, we also detected emission lines at 6.1 keV and 7.3 keV; the XSTAR model for Region II reveals no obvious candidate IDs at the velocity of the three strong lines. However, the average of the line energies coincides with the Fe XXV Heα triplet, so we identify these lines as symmetrically relativistically Doppler-split Fe XXV emission (with velocities of about 25,000 km s^{-1}). The existence of a number of faint unexplained lines near other strong emission lines detected at low energy with comparable velocity shifts (see Table 2) strengthens this interpretation.

Similar Doppler splitting was observed by *EXOSAT* during a bright flare: pulse-phased spectroscopy of the iron line suggested the existence of two line components whose separation ($\sim 0.2c$) varied with pulse phase and increased with the luminosity of the source (Dennerl 1989). The natural implication of that result is that those lines originated near the neutron star, possibly in the rapidly rotating accretion column. This would explain why the Doppler shift varied with pulse phase, and it is consistent with the visibility of the neutron star in the high state. In any case, it seems likely that this motion was dominated by the pulsar's $\sim 10^{13}$ G magnetic field (La Barbera et al. 2001).

We consider the possibility that the Doppler splitting in the state transition is also caused by the pulsar's magnetic field. Because the iron lines in the transition phase have velocity widths of order 1000 km s^{-1}, we can conclude that they do not originate in the accretion column (otherwise they would be broadened by $\sim 0.2c$ by the spin of the pulsar). However, material corotating with the magnetic field, e.g., at the inner edge of the accretion disk, could certainly be responsible for the observed lines. It is straightforward to calculate that material corotating with the neutron star at a speed of 25,000 km s^{-1} would lie at $r \gtrsim 5 \times 10^9$ cm. This result could place Region III well inside the accretion disk.

5. DISCUSSION

In this paper, we identify a number of recombination emission lines in LMC X-4; by comparing observations at two epochs, we determine the evolution of these lines with Ψ and find evidence for three emitting regions; here we discuss the implications of these results for the dynamics and geometry of this binary system.

5.1. Line Variability and Emission Regions

Our analysis of the variation of emission lines reveals clear differences in the properties of helium- and hydrogen-like N, O, and Ne in LMC X-4, which we detailed in the previous sections. We find it useful to suppose that these lines come from two different physical regions; we will argue that the disk precession model for the superorbital period, which reproduces the long-term light curve, predicts the existence of these very regions and their variability. This argument is depicted schematically in Figures 7 and 8, which show the low- and high-state geometry of LMC X-4 as seen from the orbital plane.

First, we attempt to place constraints on the physical location of Region I. Without a robust density estimate, we cannot use the ionization parameter to estimate $R_{\rm I}$. Nevertheless, in Section 4.2 we claimed that we can reasonably identify Region I with the X-ray irradiated face of the companion star or its substantial wind based on its variability; we expand on this argument here. In order to conclude that Region I must occupy a large solid angle as seen by the neutron star, we must show that shadowing by the precessing disk is unlikely to produce a constant ionization parameter and line flux over the superorbital phase.

To do so, we suppose that shadowing is important, i.e., that the illumination of Region I varies like the superorbital light curve. Between the HETGS and RGS observations, the number of ionizing photons in Region I increases by a factor of ~ 10, but its ionization parameter, ξ, remains constant. The relation

$$\xi = \frac{L}{nR^2}$$

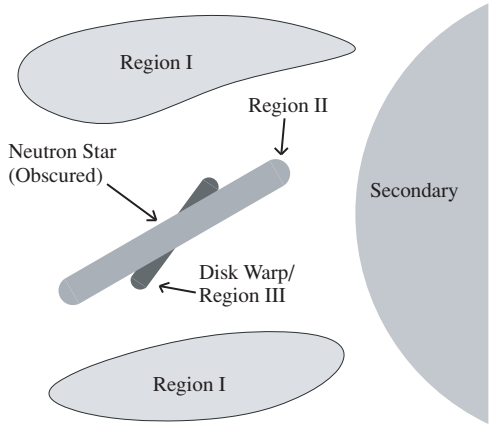

Figure 7. Cartoon of the X-ray low state of LMC X-4. The disk is viewed roughly edge-on, obscuring the neutron star. A warp protrudes from the inner disk; as the ionized surface of this warp is dragged along by the pulsar's rotating magnetic field, we observe Doppler splitting of the disk emission lines. The apparent area of the outer disk is small, so lines from Region II are weak. Note that shadowing is not particularly important in Region I. This figure should be compared to Figure 8, which shows our high-state scenario.

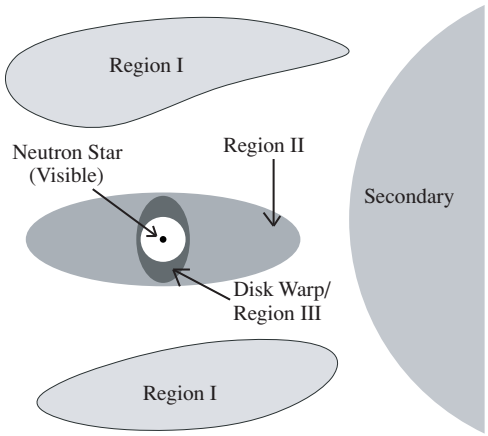

Figure 8. Cartoon of the X-ray high state of LMC X-4 to be compared with Figure 7 (the disk is more face-on now, and the pulsar is visible). Because the inclination of the disk has changed, the Doppler shifts from the inner disk/Region III are more difficult to observe. In contrast, the projected area of the disk is much larger, so we observe brighter lines from Region II. The solid angle of the wind seen by the neutron star does not change, so the line luminosity of Region I is constant. The hole in the inner disk represents the magnetosphere, where the magnetic field completely dominates the accretion dynamics.

implies that nR^2 must increase by a factor of 10 as well. But given the increase in the number of ionizing photons, Region I must also be smaller during the high state in order to produce the same line flux (in the optically thin limit). That is, the neutron star would have to illuminate a more dense, distant, and smaller region of the binary during the high state than it does during the transition.

Clearly shadowing results in a very unusual picture of Region I. The accretion geometry is vastly simplified if shadowing is unimportant, and Region I is constantly ionized by the intrinsic luminosity of the neutron star, i.e., 2.3×10^{38} erg s^{-1} (Levine et al. 2000). In this case, Region I is very likely the X-ray irradiated wind from the companion. This explanation is consistent with the low temperature of the emitting plasma as well as the small line velocities in Region I and the importance of photoionization in LMC X-4. Furthermore, a relatively steady wind could provide a solid angle which does not change over time, so that its ionization parameter and line luminosity in Region I are independent of Ψ. At present, it is difficult to distinguish between the surface and the wind of the companion. But the precession of the disk should cause periodic illumination of the face of the secondary, so a more complete high-resolution study of line emission with Ψ might be able to resolve this degeneracy and possibly constrain the inclination of the disk.

While Region I is independent of Ψ, we find that Region II, where the hot iron lines and the Lyα lines originate, is tied to the observed X-ray continuum. We argued in Section 4.3 that $R_{\rm II} \lesssim 1.5 \times 10^{11}$ cm and that Region II probably lies in the outer accretion disk, which then fills approximately 50% of the Roche lobe of the neutron star. Here, it is relatively easy to suggest how the observed equivalent width changes might occur. In the outer disk, the neutron star is always visible, so the line luminosity is constant in time (just like in Region I). However, the projected area of the disk changes periodically, leading to stronger lines when more of the disk is visible, i.e., the high state. It is also possible that the lines originate in the accretion stream, which is periodically illuminated by the neutron star so that its line luminosity is tied to the observed X-ray flux. This effect results in stronger lines during the high state of the superorbital period.

JG02 found evidence for a similar increase in emission line strengths from the low state to the short-on state in Her X-1. They suggested that the variation in line strengths might be explained by the enhanced visibility of the disk atmosphere during the short-on. While it appears that Region II is a common feature of systems with precessing accretion disks, Region I seems to be absent in Her X-1. In fact, we can use this point as further evidence that Region I is the illuminated stellar wind. Her X-1 and LMC X-4 both have very similar orbital parameters; the main dynamical difference between these systems is the mass of the companion star ($\sim$2.2 $M_\odot$ in Her X-1 and 14.5 $M_\odot$ in LMC X-4). Thus, we expect a stellar wind to contribute much more to the spectrum in LMC X-4; the absence of a Region I equivalent in Her X-1 is not surprising if our hypothesis is correct.

It seems that for a system with strong winds, the existence of two emitting regions is a natural consequence of a tilted, precessing accretion disk, which illuminates different components of the binary in different ways. One region presents a roughly constant solid angle for illumination by the neutron star, so the resulting emission lines do not vary with Ψ. A second component might precess with the disk or see the neutron star obscured, just as we do. By assuming the existence of these regions, we can sensibly decompose our observations into a physical picture of an accreting neutron star with a precessing accretion disk.

5.2. Doppler Shifts and the Superorbital Phase

We also present evidence for the relativistic Doppler splitting of the Fe XXV Heα emission line during the state transition in LMC X-4, and speculate that the lines originate in the accretion disk, where highly ionized plasma may be dragged along with the pulsar's rotating magnetic field at velocities of $\sim$25,000 km s^{-1}. We find evidence of comparably Doppler-shifted emission lines at low energy which are present during the state transition but absent in the high state. We consider here the origin of such Doppler shifts and the implications of the Doppler evolution for the geometry of the binary.

The conclusion that the Doppler splitting occurs in the accretion disk is highly dependent on the velocity field of the disk. For a Keplerian disk, orbital velocities reach $v \sim 25,000$ km s^{-1} at $r_{\rm K} \lesssim 1.9 \times 10^7$ cm. But the disk around a highly

magnetized neutron star is truncated at the radius of the magnetosphere R_M, where magnetic pressure balances the ram pressure of the gas (Frank et al. 2002):

$$R_M = 1.5 \times 10^8 m^{1/7} R_6^{-2/7} L_{37}^{-2/7} \mu_{30}^{4/7} \mathrm{cm}, \quad (2)$$

where m is the neutron star mass in solar masses, R_6 its radius in 10^6 cm, L_{37} its luminosity in 10^{37} erg s^{-1}, and μ_{30} its magnetic moment in 10^{30} G cm^3. With $m = 1.25$, $R_6 = 1$, $L_{37} = 23$, and $\mu_{30} = 10$ (from La Barbera et al. 2001), we find $R_M \sim 2.3 \times 10^8$ cm. Since the inner edge of the disk is much larger than r_K, Keplerian motion is unlikely to produce the observed Doppler shifts.

By assuming that Region III is corotating with the pulsar, we calculate $R_{III} \sim 5 \times 10^9$ cm. This is much larger than R_M, so the lines cannot originate at the very inner edge of the disk. However, R_{III} might mark the edge of the inner disk warp, and a highly ionized surface layer of the disk might continue to corotate with the magnetic field out to this radius. Thus, we conclude that the Doppler-shifted Region III lies in the inner accretion disk around LMC X-4.

To clarify this model for visualization purposes, we consider a toy accretion disk, also shown in Figures 7 and 8. Note that in these figures, the system is viewed from the orbital plane, not at the orbital inclination of $\sim 68^\circ \pm 4^\circ$ (van der Meer et al. 2007). This disk has a small but nonzero inclination with respect to the orbital plane, and precesses around the orbital angular momentum vector of the system. The inner disk is warped and slightly tilted with respect to the disk, so that the edge of the warp protrudes from the disk. The surface layer of this warp is highly ionized and corotates with the magnetic field. Furthermore, because only a small part of this warp is visible the Doppler-shifted lines are narrow, not broad, relative to the line splitting.

But we have observed LMC X-4 at multiple epochs, and it seems that the Doppler-shifted lines from Region III may not be visible at all superorbital phases. In fact, this Doppler evolution is a direct consequence of the precession of the accretion disk: the changing orientation of the disk implies a maximum radial velocity in the accretion disk during the low state and a minimum in the high state. Thus, Doppler-split lines *should* appear and disappear at different phases. It seems that we have the first dynamical confirmation of accretion disk precession as the origin of the superorbital phenomenon.

Admittedly, the nondetection of Doppler-shifted lines in the high-state RGS observation does not prove that the disk precessed from edge-on to face-on. As such, we address the possibilities that the Doppler splitting is not real (perhaps an effect of low S/N), or that we observed two distinct phenomena (and not emission lines evolving with Ψ). The Doppler-shifted Fe XXV lines are both detected at >90% confidence, so the conclusion is robust; the concern over S/N only applies to emission from low-Z species. It is tempting to suggest that because the fluxes of the Lyα lines of hydrogen-like N, O, and Ne are tied to the continuum, the Doppler-shifted lines should be most detectable in the high state as well, but there are two reasons why this is not the case.

First, the projected velocity of the accretion disk is smaller in the high state; if the disk inclination decreases sufficiently, this effect could make the Doppler-shifted lines difficult to distinguish from the stronger $v \sim 0$ line. By fitting the RXTE ASM light curve and P Cygni profiles in the UV, Boroson et al. (1999) determined a disk tilt of $31^\circ \pm 2^\circ$ off the orbital plane. Combined with the orbital inclination of 68°, this result implies that the apparent inclination of the disk warp varies from $\sim 100^\circ$ to $\sim 35^\circ$ over the superorbital phase, so that Doppler velocities in the high state should be a factor of ~ 2 smaller than in the transition. Since our grating spectra can easily resolve such velocities, the projected velocity of the disk alone cannot explain the disappearance of the Doppler lines in the high state.

Second, and more importantly, the equivalent widths of the Doppler-shifted lines should actually be anticorrelated with the continuum flux. In the high state, only the Fe Kα, the Fe XXV, and the Fe XXVI lines are visible from Region II. As the disk turns its edge to us, the continuum flux decreases and the Doppler lines appear, boosting the equivalent width of the iron line region.

This effect was already observed by Naik & Paul (2003) with the lower spectral resolution of the RXTE PCA. They found that the equivalent width of the iron complex was 650^{+45}_{-36} eV in the low state, 320 ± 30 eV in the transition, and 280 ± 20 eV in the high state. Our spectra are consistent with this result: in the transition, we find the combined equivalent width of the Fe Kα line and the Fe XXV line to be 220 ± 40 eV; including the Fe XXVI line, the equivalent width is $W_0 \sim 240$ eV. If we include the Doppler lines, W_0 increases to 300 ± 50 eV (~ 310 eV when Fe XXVI is accounted for). Thus, the RXTE data are consistent with our claim that Doppler-shifted lines are undetectable in the high state, appear in the state transition, and peak during the low state. High-resolution observations of the low state are necessary for a definitive test of this interpretation.

It may be that we observed two independent events in the state transition and the high state, but the observations can be explained with a single model. The spectroscopic interpretation of the disk precession model completely explains the variability of the emission lines in LMC X-4 with superorbital phase; all we require is that the equivalent widths of the Region II lines be independent of Ψ.

This simple requirement can be met if Region II is in the accretion disk or otherwise very close to the neutron star. Then, the observed flux in these lines will be strongly correlated with the X-ray continuum, and their equivalent widths will vary slowly with Ψ. Then as the disk precesses out of the high state, we observe additional Doppler-shifted emission lines whose velocity and flux increase into the low state before disappearing again.

6. CONCLUSION

Only a handful of XRBs are known to have persistent superorbital periods, the most famous of which are Her X-1, SS 433, SMC X-1, and LMC X-4 (Wen et al. 2006). To date, there has been very little systematic study of the superorbital variation of the strengths or positions of X-ray emission lines from the precessing accretion disk in any of these systems (grating studies of SS 433, for example, have focused on jet knots; Lopez et al. 2006). Such studies can be extremely enlightening, given the power of high-resolution spectroscopy to reveal the plasma conditions and dynamics in accreting systems.

We have presented our analysis of time-averaged grating spectra of LMC X-4 in the high state and state transition of its 30.3 day superorbital period. In both states, we detected a number of recombination emission lines; by comparing the intensities and ionization states of these lines at multiple epochs, we found evidence for two distinct emission regions, which we identified as the X-ray photoionized stellar wind (Region I) and the outer accretion disk or stream (Region II). We argued that the variability of these regions, which was similar to variability

observed in Her X-1 by JG02, was a natural consequence of accretion disk precession.

We also found evidence for relativistic Doppler splitting of the iron line in the inner accretion disk, and possible splitting in low-Z recombination lines. We suggested that these lines constitute a third region, the inner accretion disk warp. Although the Doppler shifts should be much harder to detect in the high state, the variation of the equivalent width of the iron line complex with Ψ (as measured by Naik & Paul 2003) is consistent with our conclusions.

While it is plausible that we simply observed two distinct phenomena in the different observations, the precession of the accretion disk provides a simple and coherent explanation for all the phenomena that we observed. As the disk precesses from edge-on to face-on, the continuum flux rises; emission lines in the accretion flow brighten accordingly. At this point, the neutron star is visible and pulse-phased spectroscopy reveals the rapid motion of the accretion column, dragged along by the pulsar's magnetic field. As the disk turns its edge to our line of sight, the neutron star is obscured, but the radial velocity of the corotating disk is maximized, and we observe Doppler splitting in the disk emission lines.

In this work, we have performed a new high-resolution study of X-ray emission line variability with superorbital phase in LMC X-4. Accordingly, we are able to report a new spectral confirmation of accretion disk precession as the origin of the superorbital period. The variable Doppler shifts from the inner accretion disk and the relative evolution of other emission lines in LMC X-4 are fully consistent with and predicted by the precession of the accretion disk. Future high spectral resolution observations at the peak of the high state and during the low state will go a long way toward a systematic test of this model for accretion dynamics in X-ray binaries.

We gratefully acknowledge funding support from the *Chandra* grant GO7-8044X and the Harvard University Graduate School of Arts and Sciences. We thank the referee for useful comments and Jack Steiner for many helpful discussions. This research has made use of data obtained from the High Energy Astrophysics Science Archive Research Center (HEASARC), provided by NASA's Goddard Space Flight Center.

REFERENCES

Boroson, B., Kallman, T., Blondin, J. M., & Owen, M. P. 2001, ApJ, 550, 919
Boroson, B., Kallman, T., McCray, R., Vrtilek, S. D., & Raymond, J. 1999, ApJ, 519, 191
Canizares, C. R., et al. 2005, PASP, 117, 1144
Cann, N. M., & Thakkar, A. J. 1992, Phys. Rev. A, 46, 5397
den Herder, J. W., et al. 2001, A&A, 365, 7
Dennerl, K. 1989, in Proc. 23rd ESLAB Symp. on Two Topics in X-ray Astronomy, Vol. 1: X-ray Binaries, ed. N. E. White, J. J. Hunt, & B. Battrick (Paris: ESA), 39
Dickey, J. M., & Lockman, F. J. 1990, ARA&A, 28, 215
Drake, G. W. F. 1971, Phys. Rev. A, 3, 908
Frank, J., King, A., & Raine, D. 2002, Accretion Power in Astrophysics, (Cambridge: Cambridge Univ. Press)
Gabriel, A. H., & Jordan, C. 1969, MNRAS, 145, 241
Gabriel, A. H., & Jordan, C. 1972, in Case Studies in Atomic Physics II, ed. E. W. McDaniel, M. R. C. McDowell (Amsterdam: North-Holland), 209
Giacconi, R., Gursky, H., Kellogg, E., Levinson, R., Schreier, E., & Tananbaum, H. 1973, ApJ, 184, 227
Gruber, D. E., & Rothschild, R. E. 1984, ApJ, 283, 546
Heemskerk, M. H. M., & van Paradijs, J. 1989, A&A, 223, 154
Hickox, R. C., Narayan, R., & Kallman, T. R. 2004, ApJ, 614, 881
Hickox, R. C., & Vrtilek, S. D. 2005, ApJ, 633, 1064
Houck, J. C. 2002, ed. G. Branduardi-Raymont High Resolution X-ray Spectroscopy with *XMM-Newton* and *Chandra* (Holmbury St. Mary: Mullard Space Science Laboratory)http://www.mssl.ucl.ac.uk/∼gbr/rgs_workshop/workshop_ADS_index.html
Houck, J. C., & Denicola, L. A. 2000, in ASP Conf. Ser. 216, Astronomical Data Analysis Software and Systems IX, ed. N. Manset, C. Veillet, & D. Crabtree (San Francisco, CA: ASP), 591
Ilovaisky, S. A., Chevalier, C., Motch, C., Pakull, M., van Paradijs, J., & Lub, J. 1984, A&A, 140, 251
Jimenez-Garate, M. A., Hailey,C. J., den Herder, J. W., Zane, S., & Ramsay, G. 2002, ApJ, 578, 391, JG02
Jimenez-Garate, M. A., Raymond, J. C., Liedahl, D. A., & Hailey, C. J. 2005, ApJ, 625, 931
Kallman, T. R., & McCray, R. 1982, ApJS, 50, 263
Kelley, R. L., Jernigan, J. G., Levine, A., Petro, L. D., & Rappaport, S. 1983, ApJ, 264, 568
La Barbera, A., Burderi, L., Di Salvo, T., Iaria, R., & Robba, N. R. 2001, ApJ, 553, 375
Lang, F. L., et al. 1981, ApJ, 246, L21
Levine, A. M., Rappaport, S. A., & Zojcheski, G. 2000, ApJ, 541, 194
Liedahl, D. A., & Paerels, F. 1996, ApJ, 468, L33
Lopez, L. A., Marshall, H. L., Canizares, C. R., Schulz, N. S., & Kane, J. F. 2006, ApJ, 650, 338
Mewe, R., & Schrijver, J. 1978, A&A, 65, 99
Naik, S., & Paul, B. 2002, ApJ, 579, 411
Naik, S., & Paul, B. 2003, A&A, 401, 265
Naik, S., & Paul, B. 2004, ApJ, 600, 351
Neilsen, J., Hickox, R. C., & Vrtilek, S. D. 2004, ApJ, 616, L135
Petterson, J. A. 1977, ApJ, 218, 783
Petterson, J. A., Rothschild, R. E., & Gruber, D. E. 1991, ApJ, 378, 696
Porquet, D., & Dubau, J. 2000, A&AS, 143, 495
Preciado, M. E., Boroson, B., & Vrtilek, S. D. 2002, PASP, 114, 340
Pringle, J. E. 1996, MNRAS, 281, 357
van der Meer, A., Kaper, L., van Kerkwijk, M. H., Heemsmerk, M. H. M., & van den Heuvel, E. P. J. 2007, A&A, 473, 523
Vrtilek, S. D., Boroson, B., McCray, R., Nagase, F., & Cheng, F. 1997, ApJ, 490, 377
Vrtilek, S. D., Raymond, J. C., Boroson, B., Kallman, T., Quaintrell, H., & McCray, R. 2001, ApJ, 563, L139
Wen, L., Levine, A. M., Corbet, R. H. D., & Bradt, H. V. 2006, ApJS, 163, 372
Wojdowski, P. S., Liedahl, D. A., Sako, M., Kahn, S. M., & Paerels, F. 2003, ApJ, 582, 959
Woo, J. W., Clark, G. W., & Levine, A. M. 1995, ApJ, 449, 880